

Out- versus in-plane magnetic anisotropy of free Fe and Co nanocrystals: Tight-binding and first-principles studies

Dongzhe Li,¹ Cyrille Barreteau,^{1,2} Martin R. Castell,³ Fabien Silly,^{1,3} and Alexander Smogunov^{1,*}

¹CEA, IRAMIS, SPEC, CNRS URA 2464, F-91191 Gif-sur-Yvette Cedex, France

²DTU NANOTECH, Technical University of Denmark, Ørstedes Plads 344, DK-2800 Kgs. Lyngby, Denmark

³Department of Materials, University of Oxford, Parks Road, Oxford OX1 3PH, United Kingdom

(Received 18 July 2014; revised manuscript received 10 October 2014; published 10 November 2014)

We report tight-binding and density functional theory calculations of magnetocrystalline anisotropy energy (MAE) of free Fe (body-centered-cubic) and Co (face-centered-cubic) slabs and nanocrystals. The nanocrystals are truncated square pyramids which can be grown experimentally by deposition of metal on a SrTiO₃(001) substrate. For both elements our local analysis shows that the total MAE of the nanocrystals is largely dominated by the contribution of (001) facets. However, while the easy axis of Fe(001) is out-of-plane, it is in-plane for Co(001). This has direct consequences on the magnetic reversal mechanism of the nanocrystals. Indeed, the very high uniaxial anisotropy of Fe nanocrystals makes them a much better potential candidate for magnetic storage devices.

DOI: [10.1103/PhysRevB.90.205409](https://doi.org/10.1103/PhysRevB.90.205409)

PACS number(s): 75.30.Gw, 75.50.Ss, 75.70.Ak, 71.15.—m

I. INTRODUCTION

In recent decades, higher storage densities were achieved by reducing the magnetic grains down to nanoscale. However, the magnetic stability of a nanoobject decreases proportionally to its size and the ultimate limit is reached when thermal fluctuations overcome the energy barrier to switch the global magnetization of the system. The most crucial issue in exploring ultimate density data storage (e.g., high-density magnetic recording [1] or spintronic devices) is magnetic anisotropy energy, which is defined as the change of total energy associated with a change in the direction of magnetization. One of challenges on this route towards high magnetic density storage is evidently to be able to synthesize well-ordered arrays of magnetic nanocrystals with as large magnetization and magnetocrystalline anisotropy as possible. The magnetic anisotropy energy of magnetic nanocrystals (e.g., Fe, Co, Ni, etc.) is the subject of intense experimental [2–5] and theoretical [6–11] studies but the ability to grow well-defined magnetic crystalline nanostructures is also a major issue [12–18]. This is especially the case for Fe and Co nanoclusters that can adopt various crystalline bulk structures, in particular the body-centered-cubic (bcc) and the face-centered-cubic (fcc) structures in low dimensions [15,16]. The close-packed and lowest-energy facet for bcc structure is the (110) facet, whereas it is the (111) facet for the fcc structure [19]. This is the reason for the (110) facets appearing in bcc nanocrystals [in fact, for Fe the surface energies of (001) and (110) orientations are almost the same] and the (111) facets appearing in fcc nanocrystals. The nanocrystal magnetic properties will therefore not only depend on the bulk structure but also on the facets orientation and their area.

The magnetic anisotropy contains two different parts: The first part is due to long-range magnetic dipole-dipole interactions and is called the shape anisotropy, while the second one is referred to as magnetocrystalline anisotropy energy (MAE) and originates from the spin-orbit coupling

(SOC) [20]. The latter one is the quantum effect of relativistic nature that breaks the rotational invariance with respect to the spin quantization axis. Therefore, if SOC is included, the total energy of the system starts to depend on the orientation of the spin moment with respect to the crystallographic axis.

The value of MAE per atom is extremely small in bulk cubic 3d systems (some μeV) but can get much larger in nanostructures [21,22] (some meV) due to reduced dimensionality. From theoretical point of view, there are two different methods which are extensively used in the literature for MAE calculations: (i) fully relativistic self-consistent field (SCF) calculations and (ii) the force theorem (FT) [23–25] approach. Assessing the MAE for systems containing hundreds of atoms by the first approach is especially challenging, since it requires a well-converged charge density and is very time demanding. In the second method, the MAE is given by the band energy difference (instead of the total energy difference) obtained after a one-step diagonalization of the full Hamiltonian including SOC, starting from the self-consistent scalar relativistic (no SOC) density/potential. This approach is not only much faster but also numerically very stable since the self-consistent effects with SOC can be ignored.

The objective of this paper is to investigate the MAE of Fe and Co nanocrystals, which can be grown experimentally by epitaxy, using tight-binding (TB) as well as first-principles calculations in the density functional theory (DFT) framework. The nanocrystals adopt a truncated-pyramid shape on a reconstructed SrTiO₃(001) substrate but have, however, a different bulk structure (bcc and fcc). In our theoretical study a particular emphasis is made on the local analysis of MAE. In particular, it has been found that the main contribution to the MAE comes from the basal (001) facets of pyramids. This results in strong out-of-plane (in-plane) magnetic anisotropy for Fe (Co) nanocrystals, in agreement with the study of thick Fe(001) and Co(001) slabs.

The paper is organized as follows. In Sec. II we present the experimental and theoretical methods used in this work. In Sec. III, we first present scanning tunneling microscopy (STM) observation of Co nanocrystals on SrTiO₃(001) substrate and illustrate the results of TB and DFT calculations for Co(001)

*alexander.smogunov@cea.fr

and Co(111) slabs. After that, the MAE of free Fe and Co nanocrystals will be discussed. Finally, the conclusions will be presented in Sec. IV.

II. METHODOLOGY

In the following sections we will first briefly present the main ingredients of the experimental setup to grow the cobalt nanocrystals on the SrTiO₃(001) substrate. Then in the second part the theoretical methods to calculate the MAE will be presented starting with the TB Hamiltonian and then DFT approach. In the case of the DFT formalism we will essentially concentrate on the implementation of the force theorem which we have recently incorporated in the QUANTUM ESPRESSO (QE) [26] package.

A. Experiment

We use SrTiO₃(001) crystals doped with 0.5% (weight) Nb. The crystals were epipolished (001) and supplied by PI-KEM, Surrey, UK. We deposited Co from an e-beam evaporator (Oxford Applied Research EGN4) using 99.95% pure Co rods supplied by Goodfellow, UK. Our STM is manufactured by JEOL (JSTM 4500s) and operates in ultrahigh vacuum (10⁻⁸ Pa). We used etched W tips for imaging the samples at room temperature with a bias voltage applied to the sample. SrTiO₃(001)-c(4 × 2) was obtained after Ar⁺ bombardment and annealing in UHV at 600 °C for 2 h. STM images were processed and analyzed using the home-made FabViewer application [27].

B. Theory

1. Magnetic tight-binding model

In this section, we briefly describe our magnetic tight-binding model (more details can be found in our previous publications [28,29]). The Hamiltonian is written as follows:

$$H = H_{\text{TB}} + H_{\text{LCN}} + H_{\text{Stoner}} + H_{\text{SOC}}, \quad (1)$$

where H_{TB} is a standard “nonmagnetic” and nonorthogonal TB Hamiltonian whose form is very similar to the one introduced by Mehl and Papaconstantopoulos [30]. This Hamiltonian contains three terms: the on-site atomic levels, the hopping integrals, and the overlap integrals which are written as analytic functions depending on a set of parameters. H_{LCN} is the term ensuring local charge neutrality whose expression is

$$H_{\text{LCN}}^{i\lambda,j\mu} = \frac{1}{2} [U_i(N_i - N_i^0) + U_j(N_j - N_j^0)] O_{i\lambda,j\mu} \quad (2)$$

in which N_i is the Mulliken charge of atom i and N_i^0 is the valence atomic charge. U_i is the so-called Coulomb energy of atom i whose amplitude controls the size of the charge transfer, and $O_{i\lambda,j\mu}$ is the overlap integrals between orbital $|i,\lambda\rangle$ and $|j,\mu\rangle$ (λ and μ being the s , p , and d valence orbitals). The exact value of the Coulomb energy is not important as long as it is large enough. In the following we took $U_{\text{Co}} = U_{\text{Fe}} = 20$ eV. H_{Stoner} is the Stoner-like contribution, modifying the on-site levels, that controls the spin magnetization:

$$H_{\text{Stoner}} = - \sum_{i\lambda} I_{i\lambda} \vec{M}_i \cdot \vec{S}_{i\lambda}, \quad (3)$$

where $I_{i\lambda}$ and $\vec{S}_{i\lambda}$ are the Stoner parameter and the spin operator on site i and orbital λ , and \vec{M}_i is the i th site magnetic moment.

In addition, H_{SOC} is also an on-site Hamiltonian corresponding to the spin-orbit coupling that operates on d orbitals only, written as

$$H_{\text{SOC}} = \sum_i \xi_{id} \vec{L}_{id} \cdot \vec{S}_{id}, \quad (4)$$

where \vec{L}_{id} and \vec{S}_{id} are orbital and spin moment operators with respect to the center i acting on d orbitals only. We ignore the contribution of p orbitals since its influence on the magnetic properties is negligible.

Finally, as in any mean-field approach, double counting terms must be subtracted from the sum of occupied one electron energies in order not to count twice electron-electron interactions introduced by the local charge neutrality and Stoner interaction. The total energy is then written explicitly as follows:

$$E_{\text{tot}} = E_b - E_{\text{dc}} = \sum_{\alpha} f_{\alpha} \epsilon_{\alpha} - \frac{U}{2} \sum_i [N_i^2 - (N_i^0)^2] + \frac{1}{4} \sum_{i,\lambda} I_{i\lambda} M_i^2, \quad (5)$$

where $E_b = \sum_{\alpha} f_{\alpha} \epsilon_{\alpha}$ is the band energy and f_{α} is the Fermi-Dirac occupation of state α . Note that our TB Hamiltonian depends on charges which are given by eigenfunctions. Thus, the diagonalization of this Hamiltonian should be done self-consistently.

All the parameters of the TB Hamiltonian are fitted on bulk *ab initio* data: band structure, total energy, magnetic moment, etc. The value of the Stoner parameter I_d is taken equal to 0.88 eV for Fe and 1.10 eV for Co (the s and p components of the Stoner parameter are taken as $I_s = I_p = I_d/10$). The spin-orbit constant ξ_d is also determined by comparison with *ab initio* band structure and we found that 60 and 80 meV are very good estimates for Fe and Co, respectively.

The MAE, in very good approximation, is calculated by using the FT [23–25]: First, a SCF collinear calculation without SOC is done followed by the rotation of the density matrix in the right spin direction; next, a non-SCF noncollinear calculation with SOC is performed. The MAE is obtained as the difference of band energies, $E_b^1 - E_b^2$, between two spin moment directions, 1 and 2. The appropriate decomposition of total MAE over different atomic sites i can be done within so-called “grand canonical” formulation [25]:

$$\text{MAE}_i = \int^{E_F} (E - E_F) \Delta n_i(E) dE, \quad (6)$$

where $\Delta n_i(E) = n_i^1(E) - n_i^2(E)$ is the change of the density of states at atom i for different spin moment orientations. Importantly, the Fermi level E_F of SCF calculation without SOC should be subtracted from all energies in order to suppress the trivial contribution to the local MAE due to slight charge redistribution as discussed in Ref. [25]. Note that one could refine more the MAE decomposition, defining orbital-resolved $\text{MAE}_{i\lambda}$ constructed similarly from $n_{i\lambda}^{1,2}(E)$ —the density of states on the orbital λ of the atom i . Clearly,

$\text{MAE}_i = \sum_{\lambda} \text{MAE}_{i\lambda}$ with λ going over all the orbitals of the i th atom.

2. DFT calculations

We perform *ab initio* DFT calculations using the plane-wave electronic structure package QE [26]. The SOC, crucial for magnetocrystalline anisotropy, is taken into account via fully relativistic pseudopotentials [31], describing the interaction of valence electrons with ions, which are in turn generated by solving atomic Dirac equations for each atomic type. We have implemented the force theorem in QE in the same two-step way as described above for the TB model: (i) SCF calculation with scalar-relativistic PPs (without SOC) is performed to obtain the charge density and the spin moment distributions in real space; (ii) spin moment is globally rotated to a certain direction followed by a non-SCF calculation with FR-PPs (with SOC). The change of band energy between two spin moment directions gives, as above, the total MAE.

The total MAE is decomposed over different atoms i in a slightly different way:

$$\text{MAE}_i = \int_{E_F}^{E_F^1} (E - E_F^2) n_i^1(E) dE - \int_{E_F}^{E_F^2} (E - E_F^2) n_i^2(E) dE, \quad (7)$$

where the Fermi level of one of the magnetic configurations (we have chosen the second one), E_F^2 , is subtracted under integrals and exact Fermi levels for two configurations are used as the limits of integration. In this way we avoid the reference to electronic levels of a system without SOC, since the PPs with and without SOC are not generally correlated and can produce an arbitrary shift of levels. Due to total charge conservation in this “canonical” approach, the sum of MAE_i over all atoms gives exactly the total value of MAE (calculated within the FT approach) while for the “grand canonical” scheme, Eq. (6), it was, in principle, only approximate. The discrepancy between grand canonical and canonical formulations within the TB approach is, however, very tiny since the effect of SOC on the Fermi level is negligible in the case of Fe or Co composed materials.

Since QE gives an access to real-space wave functions it is natural to define also the real-space resolved MAE as

$$\text{MAE}(r) = \int_{E_F}^{E_F^1} (E - E_F^2) n^1(r, E) dE - \int_{E_F}^{E_F^2} (E - E_F^2) n^2(r, E) dE, \quad (8)$$

where the local density of states is computed via electron wave functions in the usual way, $n^{1,2}(r, E) = \sum_{\alpha} |\Psi_{\alpha}^{1,2}(r)|^2 \delta(E - \varepsilon_{\alpha}^{1,2})$. Once again, the integral of $\text{MAE}(r)$ over all the space will give exactly the total MAE.

III. RESULTS AND DISCUSSION

In this section we will first briefly present the structural characterization of supported Co nanocrystals using STM. We then present the results of our calculations on slabs of fcc Co with orientations (001) and (111) corresponding to the facets of the nanocrystals. Next, in the second part we consider Fe

and Co nanocrystals in form of truncated pyramids with the same length-to-height ratio as in the experiments.

A. STM observations

The $\text{SrTiO}_3(001)-c(4 \times 2)$ surface [32] is used for cobalt deposition. The $c(4 \times 2)$ reconstruction was verified by STM and low-energy electron diffraction before deposition. Figure 1 shows the topography of the $\text{SrTiO}_3(001)-c(4 \times 2)$ surface following deposition of three monolayers of Co on a substrate heated to 320°C followed by a subsequent 50 min anneal at 350°C . The Co has self-assembled into similarly sized nanocrystals. The Co bulk naturally adopts a hexagonal close-packed (hcp) structure. However, epitaxial grown cobalt film can also adopt metastable fcc and bcc structures. This is why we used STM to undoubtedly determine the structure of Co nanocrystals analyzing nanocrystal dimensions. A hcp nanocrystal would have either a hexagonal top facet or a hut shape depending on the orientation. This is not the case in our STM images. Our images show that the Co nanocrystals adopt a truncated-pyramid shape. Both fcc and bcc nanocrystals can have a truncated-pyramid shape with a (100) top facet and a (100) interface. However, the Wulff construction reveals that the fcc nanocrystal has a (111) side facet. Its angle with the substrate is $\sim 54.7^\circ$. In comparison the bcc nanocrystal has a (100) side facet. Its angle with the substrate is $\sim 45^\circ$. The facet

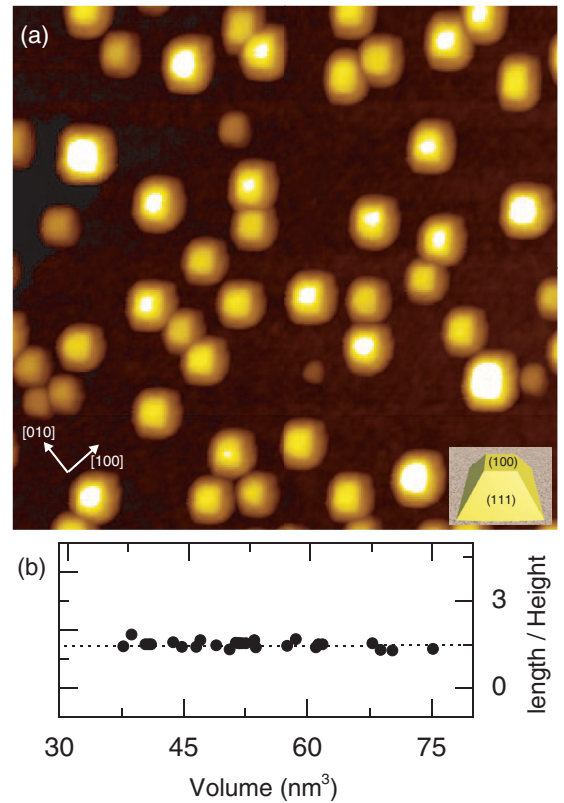


FIG. 1. (Color online) (a) Co deposition onto a 320°C $\text{SrTiO}_3(001)-c(4 \times 2)$ substrate followed by a 350°C anneal gives rise to truncated-pyramid-shaped nanocrystals as shown in the STM image, $80 \times 80 \text{ nm}^2$, $V_s = +1.0 \text{ V}$, $I_t = 0.1 \text{ nA}$. (b) The length-to-height ratio constant of Co nanocrystals.

angle is therefore a sufficient condition to distinguish the fcc from the bcc structure. In addition we measured a nanocrystal height quantization of 1.8 Å, which is consistent with the Co fcc unit-cell height. The interplanar periodicity along the (001) direction is one-half of the unit-cell dimension for both lattices (1.44 Å for bcc, 1.77 Å for fcc). The interface is therefore a (001) plane and the interface crystallography is (001)_{Co} || (001)_{SrTiO₃}, [100]_{Co} || [100]_{SrTiO₃}. As a guide to the eye we have shown in Fig. 1 (inset) a schematic illustration of a truncated pyramid. The ratio of the length (ℓ) of the top square to the height (h) of the truncated pyramids as a function of volume is shown in Fig. 1(b). The constant ratio of $\ell/h = 1.48 \pm 0.13$ suggests that these pyramidal nanocrystals have reached their equilibrium shape. The error in the ratio denotes the standard deviation of the measurements.

B. Calculations

As has been discussed above, fcc Co nanocrystals (Fig. 1) as well as bcc Fe nanocrystals [16] can be epitaxially grown on SrTiO₃(001) substrate with a remarkable control of size, shape, and structure. These crystals can contain up to several hundreds of atoms and have the form of truncated pyramids, as shown in Fig. 2, with a rather constant length-to-height ratio, ℓ/h . They, however, adopt different bulk structure, i.e., the nanocrystal facets will therefore be different because the close-packed and lowest-energy facet for bcc structure is the (110) facet, whereas it is the (111) facet for the fcc structure [19]. It is expected that the MAE of such pyramids will be dominated by the surface composed of (001) and (110) or (001) and (111) facets for Fe and Co nanocrystals, respectively. It is therefore essential to estimate first the MAE of the bulk slabs of these orientations. We present below the results for fcc Co (001) and (111) slabs, while similar results for bcc Fe slabs have already been reported recently [25].

1. MAE of Co fcc (001) and (111) slabs

The Co slabs were constructed from fcc Co with a lattice parameter of $a_0 = 3.531$ Å found from *ab initio* calculations (which is close to the experimental value of $a_0 = 3.548$ Å) and no atomic relaxations were performed. Figure 3 shows

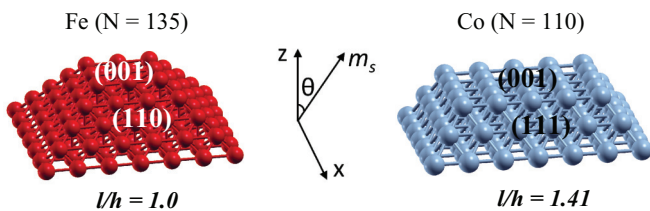


FIG. 2. (Color online) Examples of truncated-pyramid-shaped Fe and Co nanocrystals studied in the present work. The nanocrystals are made of bcc Fe and fcc Co with two types of facets: (001) and (110) for Fe and (001) and (111) for Co, respectively. Their possible size and shape are controlled by length-to-height ratio, ℓ/h , kept to ~ 1.0 (Fe) and 1.41 (Co) which are close to experimental values, ~ 1.20 (Fe) [16] and ~ 1.48 (Co). The z axis was chosen to be normal to the pyramid base and the spin moment is rotated in the xz plane forming the angle θ with the z axis.

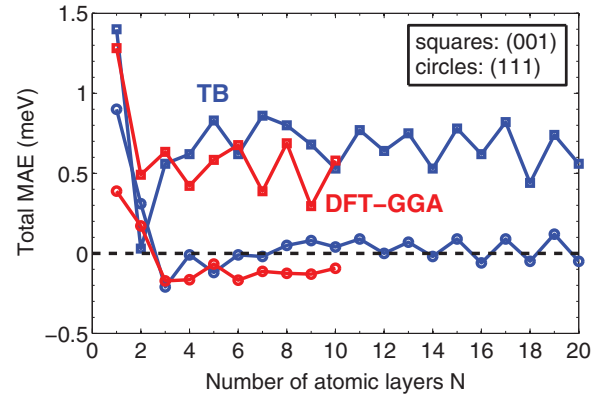


FIG. 3. (Color online) Total MAE per unit cell, $E_{\text{tot}}^{\perp} - E_{\text{tot}}^{\parallel}$, of N -atoms-thick Co slabs as a function of N . Squares and circles are for (001) and (111) slabs, respectively. TB calculations (blue) are compared with *ab initio* DFT-GGA fully relativistic calculations (red) up to $N = 10$.

thickness dependence of the total MAE of N -atom fcc Co slabs of (001) and (111) orientations. The results of both TB ($N = 1-20$) as well as *ab initio* ($N = 1-10$) calculations are presented. Note that the total MAE is obtained as the total energy difference for \vec{M} perpendicular or parallel to the atomic slabs, $\text{MAE} = E_{\text{tot}}^{\perp} - E_{\text{tot}}^{\parallel}$.

In the TB model, a mesh of 50×50 in-plane k points has been used for SCF calculations without SOC with a Marzari-Vanderbilt smearing parameter of 50 meV. In non-SCF calculations with SOC the mesh was increased to 140×140 and the smearing parameter was reduced to 10 meV which provided the MAE accuracy below 10^{-2} meV. *Ab initio* DFT calculations were carried out with the QUANTUM ESPRESSO package [26] using generalized gradient approximation (GGA) for exchange-correlation potential in the Perdew, Burke, and Ernzerhof parametrization [33]. We used 10 Å of vacuum space in the z direction in order to avoid the unphysical interactions between two adjacent slabs. Full self-consistent calculations were performed with relativistic ultrasoft pseudopotentials (no FT was employed here) and cut-off energies were set to 30 and 300 Ry for wave functions and charge density, respectively. The same mesh of 50×50 in-plane k points and the smearing parameter were employed. We find a relatively good overall agreement between TB and DFT calculations. MAE oscillations for both slabs can be clearly seen even for quite thick slabs (similar results were recently reported for bcc Fe slabs [25]). This kind of long-range oscillating behavior has been recently reported by experiments in thin ferromagnetic films (Fe and Co), and was interpreted in terms of spin-polarized quantum well states [34,35]. We notice further that for Co(001) slabs both calculations give rather similar results: The total MAE clearly favors in-plane magnetization with anisotropy energy around 0.6 meV/cell. In the case of Co(111), the MAE oscillates around zero in the TB model, while the DFT calculations predict rather small [compared to the (001) case] out-of-plane magnetic anisotropy. Note that our results compare rather well with DFT calculations of Ref. [36] done with local-density approximation for exchange-correlation functional. We further

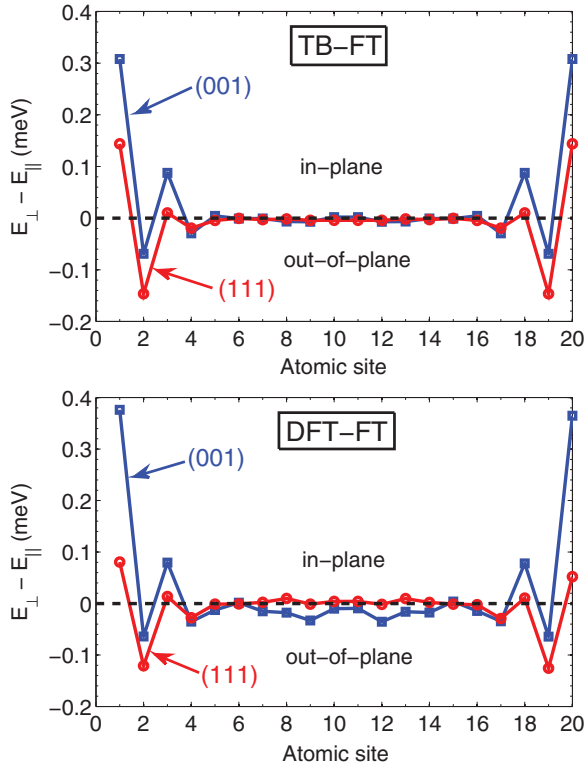


FIG. 4. (Color online) Layer-resolved MAE of Co slabs with 20 atomic layers calculated by TB (top) and DFT-GGA (bottom) within the force theorem approximation. Blue squares and red circles are for (001) and (111) slabs, respectively.

study the local decomposition of MAE of (001) and (111) Co slabs made of 20 atomic layers (Fig. 4). Here, we used the FT in TB as well as in DFT approaches as described in the previous section. A qualitatively good agreement between TB and DFT calculations is again found for both slabs with the main discrepancy appearing for the surface layers, which indicates that the TB model is presumably less accurate for low coordinated atoms. Interestingly, for both (001) and (111) slabs these surface layers possess in-plane anisotropy. The local MAE site decomposition then shows damped oscillations converging towards a tiny bulk value. However, while the MAE of the (001) slab is strongly dominated by the outermost surfaces layer, this is not the case for the (111) slab where subsurface layers cancel (and even overcome in the DFT case) the surface contribution. This leads to the large in-plane and rather small out-of-plane overall MAE for the (001) and (111) slabs, respectively, as reported in Fig. 3.

2. Free Fe and Co nanocrystals

The length-to-height ratio of different size bcc Fe and fcc Co nanocrystals can be written as $l/h = [2(n-1)]/(N-n)$ and $l/h = (n-1)/[\sqrt{2}(N-n)]$, respectively, where $N \times N$ and $n \times n$ are the number of atoms in the first (bottom) and last (up) layers of the truncated pyramid. We then selected different sizes of Fe and Co pyramids such that $l/h \sim 1.0$ for Fe (more specifically, $l/h = 1.0$ for $N = 29, 135$; 1.20 for $N = 271$; and 1.14 for $N = 620$) and $l/h = 1.41$ for Co, the

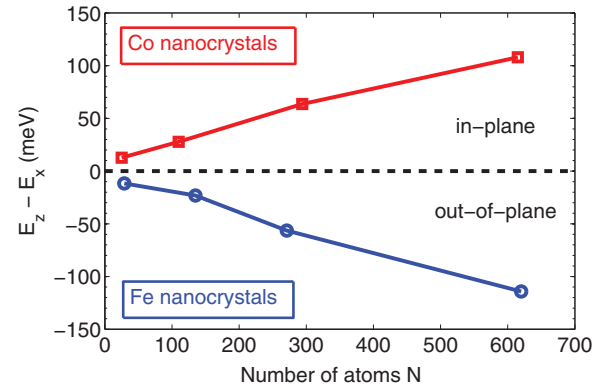


FIG. 5. (Color online) TB results: Total MAE of Co (red squares) and Fe (blue circles) nanocrystals vs the number of atoms. The size of nanocrystals was chosen so as to keep constant length-to-height ratios, 1.41 (Co) and ~ 1.0 (Fe).

values close to experimental ones, 1.20 ± 0.12 (Fe) [16] and 1.48 ± 0.13 (Co). Since the MAE in the xy plane was found to be extremely small, we kept the magnetization always in the xz plane making the angle θ with the z axis. The MAE is defined as the change in the band energy between magnetic solutions with magnetization along the z and the x axis, $\text{MAE} = E_z - E_x$. The smearing parameter of 1 meV was employed in this case of discrete level nanocrystals which allows one to achieve the accuracy of ~ 0.1 meV for the total MAE. In Fig. 5, we plot the total MAE of Fe and Co nanocrystals of growing size calculated with the TB approach. Different signs of MAE mean that out-of-plane magnetization is favored in Fe clusters, while in Co the spin moment can (almost freely) rotate in the easy xy plane which makes Fe nanocrystals better candidates for magnetic storage applications.

These results can be understood from the local analysis reported in Table I for biggest Fe ($N = 620$) and Co ($N = 615$) pyramids. One can see that the total MAE mainly originates from the lower (001) facet and its perimeter composed of least coordinated atoms. Therefore, in agreement with the previous analysis of (001) Co and Fe [25] slabs, this would favor the out-of-plane/in-plane anisotropy for Fe/Co nanocrystals, respectively. We notice, moreover, that since nanocrystals of Co are much flatter than those of Fe (as Fig. 2 illustrates), which is a consequence of bigger length-to-height ratio for Co, in the case of Co nanocrystals also the upper (001) facet, containing more atoms, gives noticeable contribution to the overall MAE. We have also checked the total MAE in the xy plane but have found it extremely small, of about 2 and 1 meV for Fe ($N = 620$) and Co ($N = 615$) nanocrystals, respectively. As mentioned in Sec. I, another important contribution to magnetic anisotropy is the so-called shape anisotropy energy. We have calculated it for biggest Fe ($N = 620$) and Co ($N = 615$) nanocrystals and have found rather small values, of about 5 and 2 meV for Fe and Co, respectively. Note that for both pyramids, the shape anisotropy favors in-plane magnetization.

We have next performed a more detailed local analysis of MAE for a smaller Co nanocrystal made of 110 atoms (shown in the right panel of Fig. 2). For such a relatively small crystal *ab initio* DFT calculation within the FT approach

TABLE I. TB results: Local analysis of MAE for Fe ($N = 620$) and Co ($N = 615$) nanocrystals. Note that the negative (positive) sign means out-of-plane (in-plane) magnetization.

	Fe ($N = 620$)			Co ($N = 615$)		
	MAE (meV)	MAE/atom (meV)	N atoms	MAE (meV)	MAE/atom (meV)	N atoms
Upper perimeter	-4.8	-0.30	16	5.9	0.18	32
Upper (001)	-3.7	-0.41	9	17.3	0.35	49
Lower perimeter	-37.5	-0.85	44	41.5	0.86	48
Lower (001)	-56.1	-0.56	100	42.0	0.42	100
Side surfaces	-15.6	-0.08	180	0.2	0.00	120
Total	-114.2	-0.18	620	108.0	0.17	615

can also be carried out and compared with TB results. Figure 6 reports atom-resolved MAE for such pyramid. The atoms of each atomic layer are numbered starting from the corner and going anticlockwise along the spiral to the center of the plane, as shown in Fig. 6(a) for the base layer. The other layers are numbered in the same way. Again, a

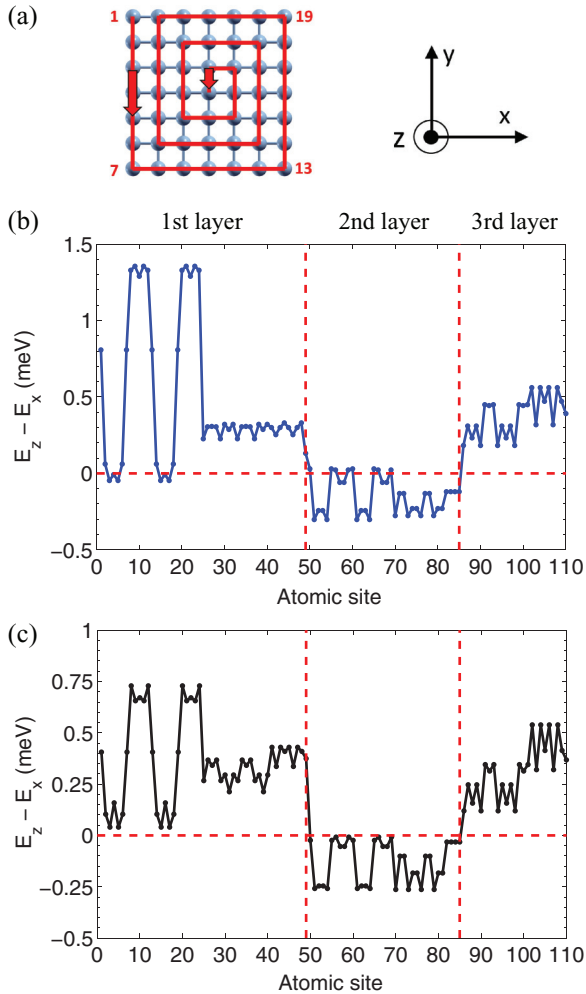


FIG. 6. (Color online) Atom-resolved MAE for Co nanocrystal made of 110 atoms: (a) trajectory for numbering the base layer atoms starting from the corner and going anticlockwise along the spiral to the center. The atoms of other layers are numbered in a similar way. (b) MAE per atom within the TB approach. (c) MAE per atom within DFT-GGA.

qualitatively good agreement has been found between the TB and DFT calculations. Interestingly, we find a sign change of MAE between atomic layers: The MAE favors in-plane magnetization for the first and third layers and out-of-plane magnetization for the middle layer of the pyramid. The MAE achieves its highest values in the middle of two first layer edges aligned with the x axis, namely, for 7-13 and 19-1 segments, and drops down to zero for two other edges. This asymmetry is due to chosen definition of $\text{MAE} = E_z - E_x$, since for the first pair of edges we compare the energies between orthogonal and parallel to the edge directions, while for the second pair—between two perpendicular directions. Clearly, in the first case the energy difference will be much bigger. Of course, if one chooses another definition of MAE, e.g., as the energy difference between the states with spin moment along the z axis and along the diagonal of the base plane, one would have more symmetric contributions from all four base edges.

To get even more insight into the local composition of MAE, we have looked at its real-space distribution as defined in Eq. (8), which can be done within the DFT approach. Such a real-space representation of MAE for the previously studied 110 atom Co pyramid is shown in Fig. 7. Interestingly, there are regions of both positive as well as negative MAE around each atom, in relative proportion which changes from layer to layer. This leads, on average, to the change of sign for atomic MAE vs the layer observed in Fig. 6. We notice moreover that positive and negative regions of MAE have different spatial

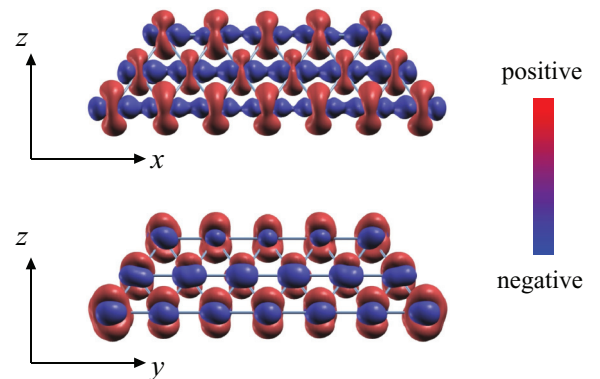


FIG. 7. (Color online) DFT calculations: Real-space distribution of MAE for Co nanocrystal of 110 atoms, side views. Two isosurfaces of positive and negative isovalues are shown in red and blue, respectively.

localization: While the first one extends out of atomic planes (along the z axis) the second one is mostly localized in the xy plane. This observation could be important when studying the MAE modification due to deposition of pyramids on various substrates.

IV. CONCLUSION

We have presented a combined TB and DFT study of magnetocrystalline anisotropy of iron (bcc) and cobalt (fcc) slabs and nanocrystals. The nanocrystals are of truncated pyramid shapes with the same length-to-height ratio as in the experiments. Thanks to the use of the force theorem that we have recently implemented in the QE package we have been able to perform a careful local analysis of the MAE in these nanostructures. The TB model is in good agreement with the DFT calculations and gives us confidence in the validity of our TB results for large nanocrystals that cannot be done within the DFT approach. We found a large in-plane anisotropy for Co(001) and a relatively small out-of-plane anisotropy for Co(111) due to cancellation from the subsurface layer in the latter case. This is in contrast with iron surfaces since Fe(001) shows a clear out-of-plane anisotropy. The densest surface shows, however, a rather small anisotropy for both elements.

These results could have a direct consequence on the magnetic stability of Fe and Co nanocrystals. Indeed, the

total MAE is of the same order of magnitude for both Fe and Co nanocrystals, but opposite in sign. This means that while the spin moment of Fe nanocrystals is fixed along the easy out-of-plane axis and needs to overcome the high MAE barrier to reverse from positive to negative direction, the magnetic moment of Co nanocrystals is allowed to rotate almost freely (with a very low in-plane anisotropy barrier) in the easy basal plane. One can thus conclude that Fe nanocrystals should be better candidates for magnetic storage applications. Our local analysis, however, indicates that the MAE of nanocrystals could be substantially altered, for instance, by their covering with a monolayer of another chemical element or by their deposition on various substrates [SrTiO₃(001), Cu, Au, etc].

ACKNOWLEDGMENTS

The research leading to these results has received funding from the European Research Council under the European Union's Seventh Framework Programme (FP7/2007-2013)/ERC grant agreement No. 259297. The authors would like to thank the Royal Society and DSTL for funding, and Chris Spencer (JEOL UK) for valuable technical support. This work was performed using HPC resources from GENCI-[TGCC/IDRIS] (Grant No. 2014096813).

-
- [1] M. Albrecht, C. T. Rettner, A. Moser, M. E. Best, and B. D. Terris, *Appl. Phys. Lett.* **81**, 2875 (2002).
 - [2] T. Balashov, T. Schuh, A. F. Takács, A. Ernst, S. Ostanin, J. Henk, I. Mertig, P. Bruno, T. Miyamachi, S. Suga *et al.*, *Phys. Rev. Lett.* **102**, 257203 (2009).
 - [3] M. Jamet, W. Wernsdorfer, C. Thirion, V. Dupuis, P. Mélinon, A. Pérez, and D. Mailly, *Phys. Rev. B* **69**, 024401 (2004).
 - [4] M. Jamet, W. Wernsdorfer, C. Thirion, D. Mailly, V. Dupuis, P. Mélinon, and A. Pérez, *Phys. Rev. Lett.* **86**, 4676 (2001).
 - [5] F. Luis, J. M. Torres, L. M. Garcia, J. Bartolome, J. Stankiewicz, F. Petroff, F. Fetta, J.-L. Maurice, and A. Vaures, *Phys. Rev. B* **65**, 094409 (2002).
 - [6] G. M. Pastor, J. Dorantes-Dávila, S. Pick, and H. Dreyssé, *Phys. Rev. Lett.* **75**, 326 (1995).
 - [7] G. Nicolas, J. Dorantes-Dávila, and G. M. Pastor, *Phys. Rev. B* **74**, 014415 (2006).
 - [8] Y. Xie and J. A. Blackman, *Phys. Rev. B* **74**, 054401 (2006).
 - [9] B. Lazarovits, L. Szunyogh, and P. Weinberger, *Phys. Rev. B* **65**, 104441 (2002).
 - [10] R. Félix-Medina, J. Dorantes-Dávila, and G. M. Pastor, *Phys. Rev. B* **67**, 094430 (2003).
 - [11] S. Sahoo, A. Hucht, M. E. Gruner, G. Rollmann, P. Entel, A. Postnikov, J. Ferrer, L. Fernández-Seivane, M. Richter, D. Fritsch *et al.*, *Phys. Rev. B* **82**, 054418 (2010).
 - [12] D. H. Kim, J. S. Yang, K. W. Lee, S. D. Bu, T. W. Noh, S.-J. Oh, Y.-W. Kim, J.-S. Chung, H. Tanaka, H. Y. Lee *et al.*, *Appl. Phys. Lett.* **81**, 2421 (2002).
 - [13] Y. Qiang, R. F. Sabiryanov, S. S. Jaswal, Y. Liu, H. Haberland, and D. J. Sellmyer, *Phys. Rev. B* **66**, 064404 (2002).
 - [14] J. Martín, J. Nogués, K. Liu, J. Vicent, and I. K. Schuller, *J. Magn. Magn. Mater.* **256**, 449 (2003).
 - [15] F. Silly and M. R. Castell, *Appl. Phys. Lett.* **87**, 053106 (2005).
 - [16] F. Silly and M. R. Castell, *Appl. Phys. Lett.* **87**, 063106 (2005).
 - [17] J. Sun, C. Wu, F. Silly, A. A. Koos, F. Dillon, N. Grobert, and M. R. Castell, *Chem. Commun.* **49**, 3748 (2013).
 - [18] H. F. Ding, A. K. Schmid, D. Li, K. Y. Guslienko, and S. D. Bader, *Phys. Rev. Lett.* **94**, 157202 (2005).
 - [19] M. Alden, S. Mirbt, H. L. Skriver, N. M. Rosengaard, and B. Johansson, *Phys. Rev. B* **46**, 6303 (1992).
 - [20] P. Bruno, *Phys. Rev. B* **39**, 865 (1989).
 - [21] P. Gambardella, S. Rusponi, M. Veronese, S. S. Dhesi, C. Grazioli, A. Dallmeyer, I. Cabria, R. Zeller, P. H. Dederichs, K. Kern *et al.*, *Science* **300**, 1130 (2003).
 - [22] S. Rusponi, T. Cren, N. Weiss, M. Eppel, P. Bulushech, L. Claude, and H. Brune, *Nat. Mater.* **2**, 546 (2003).
 - [23] X. Wang, D. Sheng Wang, R. Wu, and A. Freeman, *J. Magn. Magn. Mater.* **159**, 337 (1996).
 - [24] G. H. O. Daalderop, P. J. Kelly, and M. F. H. Schuurmans, *Phys. Rev. B* **41**, 11919 (1990).
 - [25] D. Li, A. Smogunov, C. Barreateau, F. Ducastelle, and D. Spanjaard, *Phys. Rev. B* **88**, 214413 (2013).
 - [26] P. Giannozzi, S. Baroni, N. Bonini, M. Calandra, R. Car, C. Cavazzoni, D. Ceresoli, G. L. Chiarotti, M. Cococcioni, I. Dabo *et al.*, *J. Phys.: Condens. Matter* **21**, 395502 (2009).
 - [27] F. Silly, *J. Microsc.* **236**, 211 (2009).
 - [28] G. Autès, C. Barreateau, D. Spanjaard, and M.-C. Desjonquères, *J. Phys.: Condens. Matter* **18**, 6785 (2006).
 - [29] C. Barreateau and D. Spanjaard, *J. Phys.: Condens. Matter* **24**, 406004 (2012).

- [30] M. J. Mehl and D. A. Papaconstantopoulos, *Phys. Rev. B* **54**, 4519 (1996).
- [31] A. Dal Corso and A. Mosca Conte, *Phys. Rev. B* **71**, 115106 (2005).
- [32] M. R. Castell, *Surf. Sci.* **505**, 1 (2002).
- [33] J. P. Perdew, K. Burke, and M. Ernzerhof, *Phys. Rev. Lett.* **77**, 3865 (1996).
- [34] M. Przybylski, M. Dąbrowski, U. Bauer, M. Cinal, and J. Kirschner, *J. Appl. Phys.* **111**, 07C102 (2012).
- [35] S. Manna, P. L. Gastelois, M. Dabrowski, P. Kuswik, M. Cinal, M. Przybylski, and J. Kirschner, *Phys. Rev. B* **87**, 134401 (2013).
- [36] H. Zhang, Ph.D. thesis, Dresden University of Technology, 2009.